

# Single-photon counting pixel detector for soft X-rays

Filippo Baruffaldi<sup>1,4</sup>, Anna Bergamaschi<sup>1</sup>, Maurizio Boscardin<sup>2</sup>,  
Martin Brückner<sup>1</sup>, Tim A. Butcher<sup>1,3</sup>, Maria Carulla<sup>1</sup>, Matteo  
Centis Vignali<sup>2</sup>, Roberto Dinapoli<sup>1</sup>, Simone Finizio<sup>1</sup>, Erik Fröjd<sup>1</sup>,  
Dominic Greiffenberg<sup>1</sup>, Aldo Mozzanica<sup>1</sup>, Giovanni Paternoster<sup>2</sup>,  
Nicholas W. Phillips<sup>1,5</sup>, Jörg Raabe<sup>1</sup>, Bernd Schmitt<sup>1</sup>, and Jiaguo  
Zhang<sup>1</sup>

<sup>1</sup>Paul Scherrer Institut, Forschungsstrasse 111, 5232 Villigen PSI,  
Switzerland

<sup>2</sup>Fondazione Bruno Kessler, Via Sommarive 18, 38123 Trento, Italy

<sup>3</sup>Max Born Institute for Nonlinear Optics and Short Pulse  
Spectroscopy, Max-Born-Str. 2A, 12489 Berlin, Germany

<sup>4</sup>Present address: Dectris AG, Taefernweg 1, 5405 Baden-Dättwil,  
Switzerland

<sup>5</sup>Present address: CSIRO, Mineral Resources, CSIRO 3168,  
Australia

## Abstract

Soft X-ray experiments at synchrotron light sources are essential for a wide range of research fields. However, commercially available detectors for this energy range often cannot deliver the necessary combination of quantum efficiency, signal-to-noise ratio, dynamic range, speed, and radiation hardness within a single system. While hybrid detectors have addressed these challenges effectively in the hard X-ray regime, specifically with single photon counting pixel detectors extensively used in high-performance synchrotron applications, similar solutions are desired for energies below 2 keV.

In this work, we introduce the first single-photon-counting hybrid pixel detector capable of detecting X-ray energies as low as 550 eV, utilizing the internal amplification of Low-Gain Avalanche Diode (LGAD) sensors. This detector is thoroughly characterized in terms of Signal-to-Noise Ratio and Detective Quantum Efficiency. We demonstrate its capabilities through ptychographic imaging at MAX IV 4<sup>th</sup> generation synchrotron light source at the Fe L<sub>3</sub>-edge (707 eV), showcasing the enhanced detection performance of the system. This development sets a new benchmark

for soft X-ray applications at synchrotrons, paving the way for significant advancements in imaging and analysis at lower photon energies.

## Introduction

Several imaging techniques rely on low energy X-rays, including Scanning Transmission X-ray Microscopy (STXM), full-field Transmission X-ray Microscopy (TXM), anomalous diffraction, X-Ray Magnetic Circular and Linear Dichroism (XMCD and XMLD) and Coherent Diffractive Imaging (CDI) [28, 60, 59, 21, 20]. Working at the absorption edges within the soft X-ray range between 250 eV and 2 keV offers enhanced sensitivity to specific chemical species. For instance, the K-edges of light elements such as C, O, N, F, and P, which are common in many organic and biological systems [35, 15], as well as the L-edges of 3d transition metals like Cu, Ni, and Fe, as well as the M-edges of rare earth elements, which are crucial for research on magnetic, ferroelectric, and electrode materials [25, 50, 63, 39, 64], fall within this range.

Since the early 2000s, hybrid photon-counting pixel detectors with silicon sensors have revolutionized tender and hard X-ray applications at synchrotrons, replacing previously used Charge-Coupled Devices (CCDs). These detectors have greatly advanced a range of experimental techniques, including macromolecular crystallography (MX), small-angle scattering (SAXS), CDI, and powder diffraction [24, 6], thanks to their superior dynamic range and the absence of read-out noise. Moreover, their high frame rate has enabled new methods such as fine  $\varphi$ -sliced and time-resolved crystallography [22], as well as novel scanning techniques e.g., ptychography [42], which were not feasible with earlier slower devices.

Charge integrating hybrid detectors with low electronic noise can operate at lower energies, down to a few hundred eV [26] or even into the EUV range without single photon resolution [47, 33], but they come with the drawback of limited dynamic range and more complex operation. To date, the use of single photon counting detectors has been largely limited to hard and tender X-ray energy ranges. The lowest reported energy at which Single Photon Counting (SPC) hybrid pixel detectors have been used is 1.75 keV [62]. Until now, position-sensitive SPC detectors for lower energy photons have not been available. The primary reason is that the small signals produced by single photons are nearly indistinguishable from the electronic noise of the detector [2].

Hybrid detectors consist of a sensor, which absorbs radiation and converts it into electric charge, connected to an Application Specific Integrated Circuit (ASIC) via high-density flip-chip bonding on a pixel-by-pixel basis, as illustrated in Fig. 1a. Sensors must be optimized to maximize the fraction of incident photons that are absorbed, converted into electric charge, and successfully collected. This is referred to as the Quantum Efficiency (QE). However, standard silicon sensors are typically not ideal for achieving high QE for low-energy photons. This is due to their limited ability to collect charge carriers generated just below the entrance window of the sensor. The primary advantage of the hybrid approach is that the sensor and readout electronics can be optimized independently,

with few technological constraints, as demonstrated in this work. This is a significant advantage over monolithic detectors, in which the sensor and readout electronics are integrated onto the same ASIC [52].

Monolithic detectors with an optical entrance window generally have higher QE in the soft X-ray range compared to hybrid detectors and exhibit lower electronic noise thanks to their low input capacitance [45]. Consequently, low-energy applications often use CCDs [54, 53, 43] and CMOS imagers [31, 37], despite their limitations in frame rate, dynamic range, and radiation hardness. Recent developments, however, aim to address and overcome these drawbacks [48, 18, 17].

The development of hybrid single photon counting detector systems for soft X-rays, with performance comparable to those currently achieved at higher energies, could significantly improve many experimental techniques currently limited by available detector performance [28].

This study presents the first results achieved by combining the EIGER single photon counting readout chip [19] with Low Gain Avalanche Diode (LGAD) sensors optimized for soft X-ray detection [66]. The system takes advantage of the hybrid architecture’s flexibility, substituting the standard silicon p-in-n pixel sensor with inverse LGAD devices and using their internal signal amplification to detect single low-energy photons [40, 2]. This work marks the first demonstration of a single photon counting pixel detector capable of detecting X-rays down to 550 eV. We present the performance of the system along with initial experimental results in ptychographic imaging at the Fe L<sub>3</sub>-edge at 707 eV.

## Results

**Detector description** LGAD sensors are based on an *n*-in-*p* silicon junction and incorporate an additional layer, moderately doped with the same polarity as the substrate. This region, typically created via ion implantation and referred to as the gain implant, is located just beneath the shallow surface junction. When fully depleted, this *p*<sup>+</sup> regions, exhibit an electric field high enough to enable the generation of secondary charge carriers by impact-ionization when electrons or holes travel through it. While this concept has been widely employed in avalanche photodiodes (APDs) and single-photon avalanche detectors (SPADs), LGADs are specifically designed to target a low multiplication factor *M* of approximately 5–20, avoiding dark counts while allowing segmentation. Originally proposed in the early 2010s to achieve high timing resolution in tracking detectors for high-energy physics experiments [49, 41, 9], this effect can also be used to amplify signals from low-energy photons, boosting their signal above the noise of the readout electronics [2], similar to the noise reduction achieved in Electron-Multiplying CCDs (EM-CCD) [58]. However, compared to the EM-CCD, the multiplication happens before charge collection and storage instead of at the time of readout, without affecting the frame rate. The LGAD sensors used in this study have a uniform gain layer directly beneath the entrance window, as shown in Fig. 1b, enabling a 100% fill-factor, while the fine pixel segmentation is fabricated on the opposite side of the sensor, allowing the hybridization with the

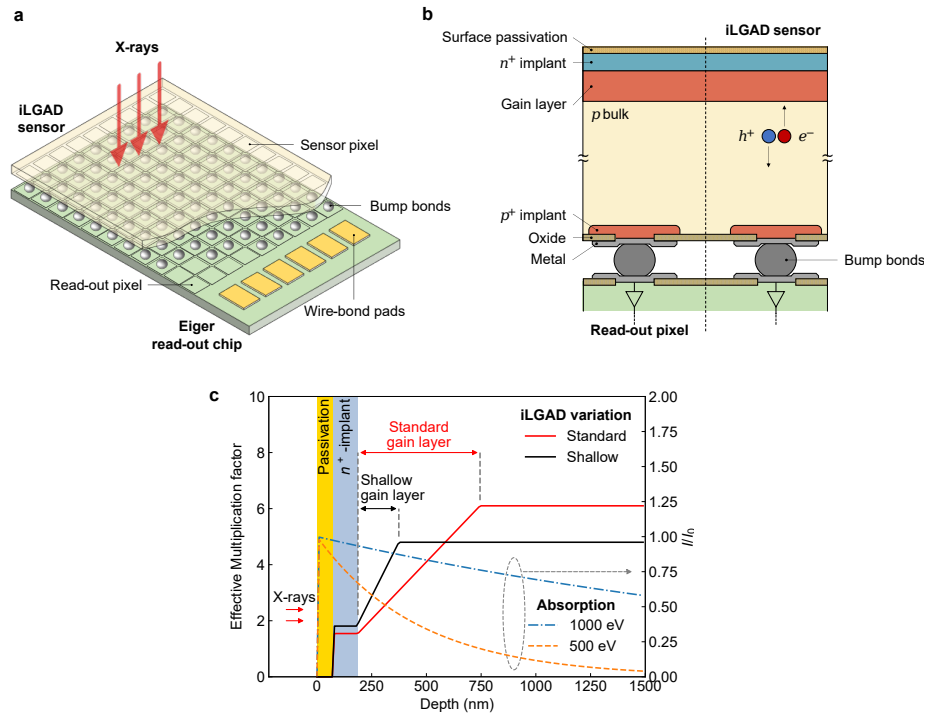


Figure 1: **Hybrid pixel detector and LGAD sensors.** **a** Layout of a hybrid pixel detector. **b** Sketch of the cross section of inverse-LGAD sensors. **c** Multiplication factor  $M$  as a function of photon absorption depth for *standard* and *shallow* iLGAD variations (data retrieved from [34]). The absorption profiles of 500 eV and 1000 eV photon beams are added for comparison.

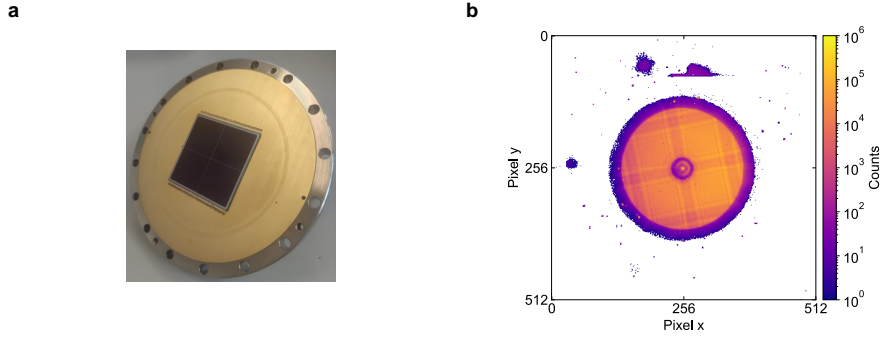


Figure 2: **EIGER-iLGAD**. **a** Picture of a  $4 \times 4 \text{ cm}^2$  inverse-LGAD sensor bump-bonded to an EIGER ASIC, mounted on a vacuum-compatible flange. **b** Image of the far-field diffraction from a Fresnel Zone Plate focusing optics projected on the detector surface acquired with a 550 eV photon beam (single frame with 1 s exposure time). Additional diffraction and scattered X-rays are visible in the background. The set threshold corresponds to  $\sim 480 \text{ eV}$ . Less than 1% noisy pixels have been masked out.

read-out electronics. These sensors are referred to in the literature as inverse-LGADs (iLGADs) [40].

Maximum charge multiplication occurs when an incident photon is absorbed in the sensor bulk, behind the gain layer. The generated electrons then drift toward the entrance window, crossing the gain layer and producing secondary electrons and holes that drift towards the entrance window and the pixel side, respectively. When photons are absorbed at shallower depths, i.e., in the n+ region or within the gain layer, charge multiplication is initiated either partially or entirely by the holes crossing the gain layer and drifting toward the pixel contacts. Since the ionization coefficient of holes is lower than that of electrons in silicon, this results in a lower effective multiplication factor  $M$ , as illustrated in Fig. 1c, which shows  $M$  as a function of the depth of the photon absorption. To address this, iLGAD variations with a shallower gain layer were investigated. In the *standard* design, the gain layer extends to a depth of 800 nm, while in the *shallow* design, it reaches about half of that depth, thus increasing the fraction of electron-initiated events [34].

To overcome the poor QE of conventional silicon sensors in the soft X-ray range, a novel entrance window process has been developed [66]. This optimized entrance window is based on a customized doping profile and includes a thin  $\text{SiO}_2$  and  $\text{Si}_3\text{N}_4$  passivation layer on the surface, enhancing charge collection efficiency and achieving a QE of up to 55% at 250 eV, limited only by the thickness of the passivation layer [34, 11]. In comparison, conventional sensors typically achieve a QE of less than 5% at this energy [62].

These novel LGAD sensors are combined with the  $75 \mu\text{m}$  pitch single photon counting EIGER ASIC, widely used in hard X-ray applications

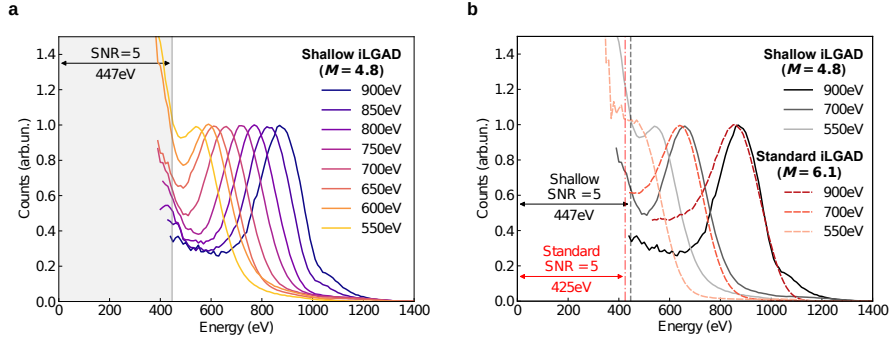


Figure 3: **Pulse-height distributions.** **a** Calibrated pulse-height distribution as a function of the X-ray photon energy for the *shallow* iLGAD variation,  $M=4.8$ . The spectra are obtained as average after a pixel-wise calibration, and normalized to the peak integral. The gray band and horizontal arrow indicate the level at which a SNR of 5 is achieved, considering the ASIC settings optimized for 550 eV. The ASIC settings have been optimized for the individual energies. **b** Comparison of the calibrated pulse-height distributions obtained using a *standard* and a *shallow* iLGAD sensor variation at 900 eV, 700 eV, and 550 eV. The ASIC settings have been optimized for the individual energies, and iLGAD sensor variations. Vertical lines indicate the levels at which a SNR=5 is reached for each of the two sensor variations, considering the ASIC settings used for 550 eV. The curves have been normalized at the peak integral.

worldwide [12, 67, 30, 29, 1]. Additional details about the EIGER ASIC are available in the Methods section. The system comprises  $2 \times 2$  ASICs bump-bonded to a  $275 \mu\text{m}$  thick iLGAD sensor with  $512 \times 512$  pixels, covering an area of  $4 \times 4 \text{ cm}^2$ , as shown in Figure 2a. The sensors used in this study, fabricated by Fondazione Bruno Kessler (FBK, Trento, Italy), are the largest LGAD sensors reported to date. Figure 2b demonstrates the detector’s capability to detect photons down to energies of 550 eV by imaging the far field diffraction from a Fresnel Zone Plate focusing optic at this low energy, an achievement unmatched by any single photon counting detector to date. The estimated Detective Quantum Efficiency (DQE) is estimated to be about 30% (see section ) and logarithmic color scale emphasizes both the absence of noise and the large dynamic range.

**Performance of the system** Figure 3a shows the average calibrated pulse-height distributions measured for a *shallow* iLGAD sensor variation, with multiplication factor 4.8, with photon energies between 550 eV and 900 eV. Although detectable, photon energies below 550 eV are not shown since at these energies the Signal-to-Noise Ratio (SNR) and the Detective Quantum Efficiency (DQE) decreases considerably (see Fig. 5). Additionally, at lower energies the multiplication is mostly triggered by holes, resulting in a lower effective gain, since the majority of the photons convert before or in the gain layer. Consequently, signals from hole-triggered

multiplication are often indistinguishable from noise. The main peak in the curves, results from photons absorbed in the sensor bulk, behind the gain layer, and undergoing electron-initiated multiplication, with the totality of the charge collection in a single pixel. The flat region preceding the peak is caused by two factors: i) photons that convert at a shallower depth, which results in a lower charge multiplication factor, and ii) charge-sharing effects, where the generated charge is distributed across multiple readout pixels [36]. In the graph, the threshold level at which a Signal-to-Noise ratio of 5 is reached is highlighted, which is equal to 447 eV, for this variation.

Figure 3b compares the average pulse-height distributions for *standard* and a *shallow* iLGAD sensors (with  $M = 6.1$  and  $M = 4.8$ ) respectively at 550 eV, 700 eV, and 900 eV. The *standard* iLGAD variation shows an increased flat region below the full-energy peak, as fewer photons convert within the thinner gain layer. The shift towards lower energies of the peak position, in the case of the *standard* variation, can be attributed to the same effect, as a smaller fraction of the events undergoes an optimal multiplication. Thanks to the higher  $M$ , a SNR of 5 is reached at a marginally lower threshold, 425 eV. However, a smaller fraction of photons will be detected, compared to the *shallow* variation (see Fig. 5). The ratio of photons undergoing electron-triggered multiplication to those absorbed before or within the gain layer influences the DQE of the detector. Charge-sharing effects are expected to be consistent across iLGAD variations, as they are influenced primarily by pixel size and charge collection time, which are determined by sensor thickness, bias voltage, and X-ray energy [5]. The calibration method and the procedure for obtaining the average pulse-height distributions shown in Fig. 3 are detailed in the Methods section.

Fig. 4a shows the noise as a function of the calibration gain  $\mathcal{G}$  of the detector, which includes the combined gain of the readout electronics and the iLGAD multiplication factor  $M$ . The calibration gain is the conversion factor between signal amplitude and photon energy and it is expressed in mV/eV.  $\mathcal{G}$  depends on the preamplifier gain settings of the ASIC, and on the LGAD multiplication factor  $M$  (see Methods). The noise is measured as Equivalent Noise Charge (ENC), expressed in electrons, which is the input signal required to produce an output equal to the rms noise. The gain and noise values are extracted for each pixel and averaged. The error bars indicate the standard deviation of the pixel distribution (see Supplementary Material for details). A higher  $\mathcal{G}$  is generally linked to a lower effective noise, as visible in Fig. 4a, and the use of LGADs significantly improves performance compared to an EIGER ASIC paired with a conventional silicon sensor under the same settings, as the signal is further amplified by the multiplication process in the sensor. A fit with a reciprocal function is added to the plot.

Ideally, the noise reduction of an LGAD sensor with respect to a conventional Si sensor scales linearly with  $M$ , when the same ASIC settings are used. For instance, with an LGAD sensor providing a  $M \sim 3$ , the effective noise is reduced from 90  $e^- rms$  to less than 30  $e^-$ . However, with higher  $M$ , the noise reduction becomes less efficient, due to factors such as the excess noise from the multiplication process and the increased

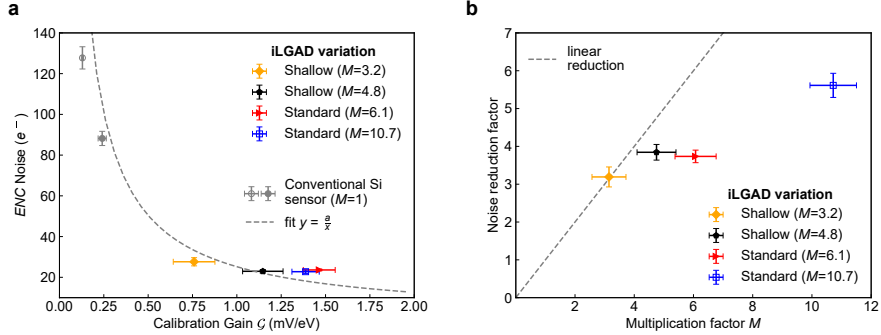


Figure 4: **Noise performance.** **a** Effective noise as a function of calibration gain  $\mathcal{G}$ , of 4 iLGADs samples of both *standard* and *shallow* variations, compared to a conventional silicon sensor. The data points are fitted with a function  $y = a/x$ , as the Effective Noise is expected to have an inverse relation with the calibration gain  $\mathcal{G}$ . For the data points two different settings of the EIGER ASIC are used, differentiated in the plot by filled or empty markers. **b** Noise reduction factor as a function of the LGAD multiplication factor  $M$ , with respect to a conventional silicon sensor, for the four iLGADS samples of both variations. The dashed line indicates the ideal case where the noise reduction scales linearly with  $M$ ; the data points fall below this trend and are tabulated in the Supplementary Materials.

leakage current [16]. In this work, effective noise levels as low as  $23 e^- rms$  were achieved. As shown in Figure 4b, for  $M$  lower than 4, the noise is effectively reduced by a similar factor. However, as  $M$  increases, the noise improvement becomes sub-linear. For instance, at a gain of around 5, the noise reduction is approximately a factor of 4, whereas for  $M \sim 11$ , the noise is reduced by less than a factor of 6. There is no noticeable difference in noise reduction between the *shallow* and *standard* iLGAD designs. However, a thicker gain layer typically enables a higher multiplication factor.

The SNR as a function of photon energy is shown in Fig. 5a. The average of the SNR calculated for each individual pixel is shown with the error bars indicating the standard deviation of the distribution. Both *standard* and *shallow* sensor variations achieve an SNR above 10 at about 850 eV. At 550 eV, the estimated SNR values are about 5.4 for both variations. The SNR varies only marginally between the two variations over the explored energy range. The optimal performance of a single photon counting detector is obtained for an  $SNR \geq 10$  [4] and the threshold set at half of the photon energy. An optimal threshold at half of the photon energy, and  $SNR \geq 5$ , can therefore be set only above 800 eV. While the detector can operate with a lower SNR, this compromises the Counting Efficiency (CE) because the threshold must be set higher than half the photon energy. Additional details are provided in the Supplementary Material.



Fig. 5b shows the calculated Detective Quantum Efficiency (DQE) of the detector as a function of photon energy, at zero spatial frequency. The DQE combines the QE of the sensor and the CE with the threshold set at the greater of either half the incoming energy or the energy at which SNR=5. It is a key figure of merit that describes how effectively a photon is converted into useful information in the final image. The calculation is based on the iLGAD parameters, measured in [34], and on the measured noise levels and multiplication values from this work. The ideal Counting Efficiency  $CE_{ideal}$  is defined as the fraction of total incident photons detectable with a threshold at half of the photon energy, assuming a noiseless electronics and 100% QE, it depends on the charge sharing and is only affected by photon loss in the pixel corners [23]. For a detector with pixel pitch as the ones used in this study, the maximum CE is approximately 93%; the charge-sharing effect has been estimated from the average pulse-height distributions in Fig 2, with a procedure reported in Supplementary Materials.

For SNR>10, i.e., down to 800 eV, the DQE of the detector is close to the ideal value, given by the product between the QE of the sensor and the ideal CE, indicated as  $DQE_{ideal}$  in Fig. 5b. The DQE decreases with the energy, due to the lower QE of the sensor, as well as to a reduced counting efficiency. This reduction in CE arises from the inability to set the threshold at half the photon energy because of noise constraints. Additionally, at low energies, a higher proportion of photons are absorbed before or within the gain layer. Consequently, the *shallow* variation, with its thinner and shallower gain layer, achieves a higher DQE over the whole energy range.

**Ptychographic imaging** Ptychography is a scanning CDI method that has been highly successful with hard X-rays, with resolution far surpassing the pixel size of the detector and the focal spot of the beam [42]. Single photon counting detectors are routinely used in this application, providing the high dynamic range needed to detect both the strong signals from the diffraction cone and the weak signals at high Q-values. A fast frame rate is essential to match the high flux provided by modern X-ray sources and to facilitate rapid scanning [14]. Moreover, burst ptychography using a multi-kHz framing detector promises to further improve the resolution limits of this technique by reducing the effects of mechanical instabilities [1]. The development of the EIGER-iLGAD detector opens possibilities for extending high-throughput, high-resolution ptychographic imaging into the soft X-ray energy range.

An EIGER-iLGAD detector with *shallow* sensor variation was installed at the SIM beamline of the Swiss Light Source (Paul Scherrer Institute, Switzerland) [44] for commissioning and proof-of-principle experiments until the facility shut down for upgrades in September 2023. The detector is now used in the SOPHIE endstation, currently installed at the SoftiMAX beamline at the MAX IV synchrotron in Lund, Sweden [51], where it is routinely available to the synchrotron user community.

In order to demonstrate the suitability of the detector for CDI, a permalloy ( $Ni_{81}Fe_{19}$ ) Siemens star of 150 nm thickness was imaged by soft X-ray ptychography at 707 eV, where the DQE of the detector is

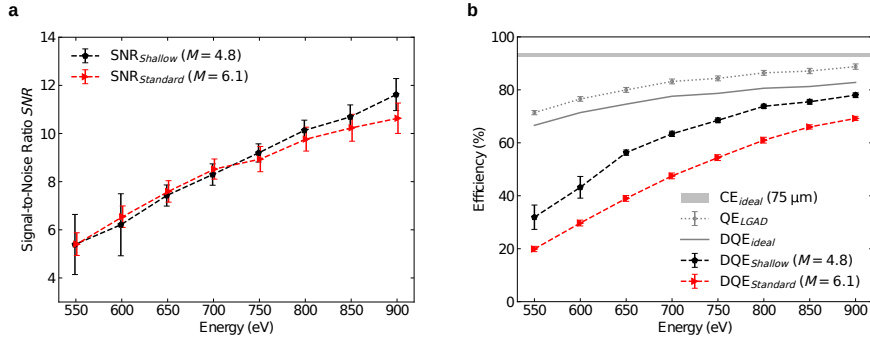


Figure 5: **SNR and DQE** **a** Measured Signal-to-Noise ratio for both iLGAD variations. The SNR is calculated for each single pixel and averaged, the error bars indicate the standard deviation of the pixel distribution. **b** Calculated Detective-Quantum-efficiency at zero spatial frequency as a function of photon energy. The reported DQE represents the fraction of incoming photons that can be counted; the threshold is considered set at 50% of the incoming photon energy for 800 eV and higher, and at SNR=5 for lower energies. The ideal Counting Efficiency ( $CE_{ideal}$ ) takes into account only the loss of counts due to charge-sharing, when the threshold is set at half of the incoming energy, considering an ideal QE and noise-less electronics.  $QE_{LGAD}$  is the measured Quantum Efficiency [34].  $DQE_{ideal}$  is the product between  $CE_{ideal}$  and  $QE_{LGAD}$ , i.e., the ideal Detective Quantum efficiency achievable by an LGAD sensor, without losses due to the multiplication process and considering a noiseless electronics. Additional details on the SNR estimation and DQE calculation can be found in the Supplementary Material.

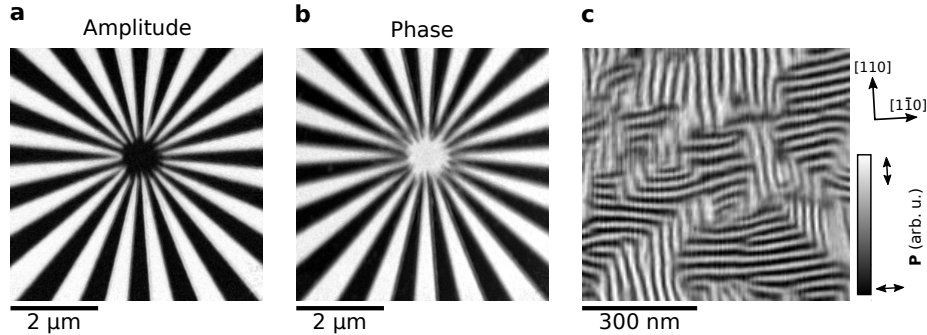


Figure 6: **Ptychographic images.** **a** Amplitude and **b** Phase ptychographic images of a 150 nm thick permalloy Siemens star images. **c** X-ray magnetic linear dichroism image (phase contrast) showing the in-plane projection of the ferroelectric polarisation ( $\mathbf{P}$ ). Large 500 nm multiferroic domains are visible, each of which contains a spin cycloid (64 nm period) in a 80 nm freestanding  $\text{BiFeO}_3$  (001) film. The crystallographic axes of the  $\text{BiFeO}_3$  film are indicated above the color bar. The contrast indicates both the direction of  $\mathbf{P}$  in the  $\text{BiFeO}_3$  film and delineates the spin cycloid coupled within the multiferroic domains (see [7, 8] for details). All images were acquired with an X-ray energy of approximately 707 eV (Fe  $L_3$ -edge).

approximately 50%. The resulting amplitude and phase images are displayed in figures 6a and b, respectively. The spatial resolution achieved in this image was estimated using Fourier Ring Correlation (FRC) between two identical ptychographic scans [3], suggesting a resolution of 10.6 nm with a 1 bit threshold.

Figure 6c demonstrates the detector’s performance in an X-ray linear dichroism (XLD) image of a freestanding  $\text{BiFeO}_3$  (001) film. Additional images of the multiferroic domains structure in  $\text{BiFeO}_3$ , acquired with the detector presented here, have been published in [7, 8]. The results in [8] demonstrate that the EIGER-iLGAD detector is also capable of operation at the O K-edge (530 eV), even below 550 eV. However, while it remains functional at these lower energies, there is a reduction in DQE and a lower spatial resolution in the reconstructed image.

## Discussion

The presented system, combining the EIGER single-photon counting pixel ASIC with custom-developed LGAD sensors, successfully extends hybrid detector capabilities into the soft X-ray energy range, pushing the lower limit for single-photon resolution down to approximately 550 eV. This system achieves a SNR above 5, without compromising performance in frame rate, dynamic range, or noise-free operation, that are intrinsic of the photon-counting architecture. The energy range of the presented detector can be even pushed down to lower energies, by sacrificing its DQE.

In general, the *shallow* iLGAD design offers higher DQE across all X-ray energies. Further increasing the  $M$  while maintaining low noise performance could be beneficial for extending detection to even lower energies.

Despite the promising results, further developments are needed before this detector can fully meet the requirements of the entire soft X-ray imaging community. Improvements in both pixel and sensor yield are essential. Currently, the pixel yield is around 97%, with significant variability observed between different sensors, likely due to non-uniformity of the multiplication factor, as discussed in [27]. The pixel yield declines rapidly at higher temperatures and lower bias voltages, suggesting that leakage current may be causing saturation in the analog chain. Reducing the leakage current through sensor technology advancements would enable detection at lower photon energies and reduce effective noise. Enhanced cooling and optimized biasing could similarly improve performance. Additionally, the fabrication of large-area iLGAD of  $4 \times 4 \text{ cm}^2$  with high production yield still has to be demonstrated, considering that the first prototyping batch showed a yield limited to about 30%. A higher yield is necessary to reliably build multi-megapixel detectors, as is standard practice with conventional silicon sensors for hard X-rays.

Additional improvements can be achieved through advances in both readout electronics and iLGAD sensor technology. While reducing noise in single photon counting detectors to improve the minimum detectable energy is challenging, and likely limited to a 30-50% improvement in the short term, significant progress is being made to increase count-rate capabilities [65], a crucial step for operating single photon counting detectors at diffraction-limited light sources currently under construction worldwide. The high gain provided by LGADs enables faster signal shaping, which is essential for achieving the required count rate capabilities.

In the future, even lower energies could be achievable through the development of a lower-noise photon-counting ASIC paired with LGAD sensors. Simultaneously, advancements in LGAD technology are underway to increase the  $M$  up to 20, enabling detection at lower energies and improving sensor QE by further thinning the entrance window. From the sensor perspective, the QE can be enhanced by reducing the passivation layer on the entrance window, while a higher counting efficiency may be achieved with even shallower and thinner gain implants. However, increasing  $M$  to access lower energies is effective only if the leakage current, which raises shot noise and decreases pixel yield, remains controlled.

New generation single photon counting LGAD detectors will be instrumental for exploiting the higher coherence provided by 4<sup>th</sup> generation light sources at soft and tender X-ray beamlines with the goal of extending to the EUV energy range with sensors with higher multiplication factors. Moreover, iLGAD sensors combined with charge integrating readout find applications at X-ray Free Electron Lasers [27]. The possibility of applying position interpolation methods open new perspectives also for high resolution imaging, including Resonant Inelastic X-ray Scattering (RIXS), where single photon detection combined with high spatial resolution is essential and high frame rate detectors are lacking. The advancement of single photon counting detectors for soft X-rays opens new frontiers in low energy photon science applications, offering unparalleled sensitivity and

precision that promises to revolutionize fields from biological microscopy to materials science by enabling detailed insights at lower energies than ever before.

## Methods

**iLGAD sensors** Low Gain Avalanche Diodes (LGADs) are silicon-based sensors that include an additional moderately-doped implanted region (gain implant) of the same type of the substrate, where charge carriers are accelerated by a strong electric field (of the order of 300 kV/cm), initiating impact ionization and achieving a charge multiplication of approximately a factor of 10. The multiplication factor is mostly determined by the doping profile and concentration of the gain implant. The original LGADs developed for high-energy physics [9] feature a coarse segmentation, with about 1 mm pitch pixels and the gain implant matching the pixel layout. To prevent breakdown at pixel edges, termination structures are needed to create gain-free regions, which effectively reduces the fill-factor i.e., the proportion of the pixel where the charge produced by X-rays undergoes multiplication [10]. Various LGAD technologies aim to minimize or eliminate this limitation [13]. For the soft X-ray sensor presented here, an inverse-LGAD (iLGAD) design was used, featuring a uniform gain layer on the entrance window of the sensor [40]. The sensors used in this study are 275  $\mu\text{m}$  thick. The sensors are fabricated using  $p$  silicon wafers, with  $p^+$  pixel implants. A  $n^+$  implant on the entrance window side forms the collecting junction, and the additional  $p^+$ -type gain implant is formed just underneath the junction. Such a gain implant is not-segmented and it extends through the full sensor area, as shown in figure 1b. The sensors operate with hole collection, where holes drift toward the pixel while electrons move in the opposite direction (see Fig. 1b). The sensors were operated with a bias voltage of 300 V, although due to possible voltage drops along the bias line, the effective voltage reaching the sensors may be lower. The bias voltage has a small effect on the multiplication factor, while it can affect charge sharing.

The impact ionization can be triggered by electrons, when a photon is absorbed after the gain layer in the  $p$ -type bulk of the sensor, or by the holes, if a photon is absorbed before the gain layer. A mix of these two processes occurs when a photon is absorbed within the gain layer. Holes have a multiplication factor that is 2 to 4 times lower than electrons, due to their lower impact ionization coefficient, depending on the electric field and the doping profile of the gain layer. The multiplication factor values  $M$  for iLGAD sensors refer specifically to electron-triggered multiplication [34]. The *standard* iLGAD variation has a gain layer thickness and doping profile similar to LGADs designed for tracking applications, while the *shallow* variation features a thinner gain layer closer to the surface to reduce hole-initiated multiplication. The iLGAD sensors presented here have an entrance window optimized for soft X-rays, featuring a thin  $\text{SiO}_2$  and  $\text{Si}_3\text{N}_4$  passivation layer, for a total of about 80 nm, instead of the aluminum layer used in conventional silicon sensors. Additionally, the doping species, profile, and concentration in the  $n^+$ -implant have been

optimized. A new batch of sensors with even thinner passivation is under development, which is expected to further enhance the QE.

**EIGER single photon counting read-out** The EIGER is a photon-counting ASIC, developed at PSI for diffraction experiments at synchrotron light sources. It features a 75  $\mu\text{m}$  pixel pitch, with each ASIC comprising  $256 \times 256$  pixels and covering an area of  $2 \times 2 \text{ cm}^2$  [19]. Each pixel includes a low-noise charge preamplifier and shaper with adjustable gain and speed, a comparator with a globally set threshold, a 6-bit DAC (trim bits) to correct pixel-by-pixel inhomogeneities, and a 12-bit counter. The comparator in each pixel is triggered whenever the shaper signal exceeds the threshold, counting events in the pixel counter, which is read out after the exposure time. The gain of the analog chain is controlled by adjusting the preamplifier feedback resistance, set through a gate voltage (*vrpreamp*). This adjustment allows a trade-off between noise (as low as  $\sim 100 e^-$  ENC r.m.s. [57]) and count-rate capability (up to  $\sim 1 \text{ MHz/pixel}$  [46]). The 12-bit counter can be extended to 32-bits in firmware with minimal dead time between sub-frames, and the bit depth can be adjusted to reach frame rates up to 22 kHz in 4-bit mode.

In this study, the detector is built by arranging  $2 \times 2$  ASICs ( $4 \times 4 \text{ cm}^2$ ,  $512 \times 512$  pixels) bump-bonded to a single sensor of the same area. A 150  $\mu\text{m}$  gap between adjacent ASICs creates a cross-shaped blind area, visible in Figure 2a. Additionally, along the sensor edges, the outer 9 pixels are replaced by guard-ring structures to prevent breakdowns, making them blind. In this work, the threshold voltage is set uniformly across all four ASICs in the detector system, and the trim-bits correction is not used. The sensor and electronics are operated in vacuum at pressures lower than  $10^{-5}$  mbar and at  $-28^\circ\text{C}$ , using a liquid chiller. Lower temperatures help reduce sensor leakage current and increase the LGAD multiplication factor, thereby enhancing the SNR [66, 27].

The detector is connected to the readout board via flat-band cables and a vacuum flange patch panel, limiting the readout clock speed to half of its nominal value and capping the maximum frame rate at 10 kHz.

**Calibration** The characterization and calibration of the detector are performed via threshold scans, where counts are measured as a function of the comparator threshold using a constant-flux monochromatic photon beam. An example of the resulting *s*-curves is shown in Figure 7a. Pulse-height distributions are obtained as the derivative of the threshold scans. The lower part of figure 7a presents uncalibrated pulse-height distributions for various iLGAD variations with different multiplication factor *M*, at 900 eV, averaged over a large number of pixels; the preamp settings of the EIGER ASIC are the same for all the datasets.

The threshold scans can be fitted on a pixel-by-pixel basis using an *s*-curve function, as described in [32]. This fit enables extraction of the photon count, full-energy peak position, noise level, and fraction of shared charge. Pixel-wise calibration is performed with a linear fit of the peak position in the pulse-height distribution as a function of the beam energy. Figure 7b shows the position of the full-energy peak as a function of the

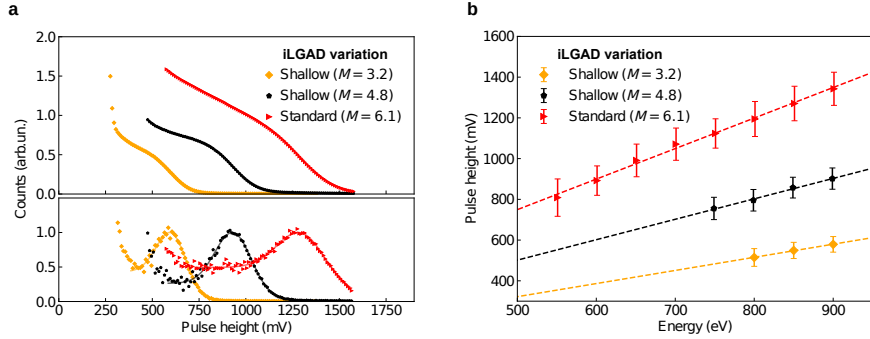


Figure 7: **Energy calibration.** **a** Top pad: uncalibrated average threshold-scan (*s*-curves) for three different sensor variations, with photon energy of 900 eV, and same settings of the EIGER ASIC; bottom pad: Uncalibrated average pulse height distribution, obtained as a derivative of the measured *s*-curves. The markers represent experimental data and the continuous lines the fit (see Eq. 1 in Supplementary Material) **b** Correlation between photon energy and signal amplitude for three iLGAD variations of different  $M$ ; the values are calculated as average over multiple pixels and the error bars represent their standard deviation; the energy calibration is performed via a linear fit (dashed lines), where the slope is  $\mathcal{G}$ .

photon energy, with linear fits; the data points represent the average and the error bars the standard deviation of the distribution of the pixels. The calibration gain of the detector  $\mathcal{G}$  is defined by the slope obtained from this fit and depends on both the gain settings of the pixel preamplifier and the multiplication factor of the LGAD sensor  $M$ .

The noise value, derived from the *s*-curve fit, is converted using the calibration gain  $\mathcal{G}$ . It represents the standard deviation of the calibrated photon peak and is expressed in units of electron-hole pairs, which correspond to 3.6 eV per pair in silicon. With a fixed  $\mathcal{G}$ , a higher  $\mathcal{G}$  generally yields a lower noise level (see Fig. 4a), though it comes at the expense of count-rate capability. The  $M$  of an LGAD sensor can be estimated as the ratio of the average conversion gains to that measured with a conventional silicon sensor, under the same preamplifier gain settings (see Supplementary Material).

**Ptychography** Ptychographic imaging with the EIGER-iLGAD detector was performed using the SOPHIE (Soft X-ray Ptychography Highly Integrated Endstation) endstation. The sample to detector distance was 96 mm. The X-ray beam, tuned to the Fe  $L_3$ -edge (707 eV), was focused to a 900 nm FWHM spot on the sample using a 500  $\mu\text{m}$  diameter line doubled iridium Fresnel zoneplate with 20 nm outer zone width. A step size of 200 nm was chosen for the ptychographic scan on a Fermat spiral trajectory. The dwell time for each position was 220 ms, resulting in a total acquisition time of approximately 3 minutes for a  $5 \times 5 \mu\text{m}$  scan area.

The XLD phase image of the BiFeO<sub>3</sub> film shown in Fig. 6c was acquired with a 50 nm step size and 400 nm FWHM illumination.

The reconstruction of the images was performed with 1200 iterations of difference-map [55] and 200 iterations of maximum-likelihood refinement [38] implemented in the Ptychoshelves software package [61]. The illuminating wavefront was reconstructed with three probe modes [56]. The XLD phase image in Fig. 6c was computed by subtracting the drift corrected phase images obtained with horizontal and vertical X-ray polarization.

## Data availability

The data that support the findings of this study are available from the corresponding author, A.B., upon reasonable request.

## References

- [1] Tomas Aidukas, Nicholas W Phillips, Ana Diaz, Emiliya Poghosyan, Elisabeth Müller, Anthony FJ Levi, Gabriel Aeppli, Manuel Guizar-Sicairos, and Mirko Holler. High-performance 4-nm-resolution x-ray tomography using burst ptychography. *Nature*, 632(8023):81–88, 2024.
- [2] Marie Andrä, Jiaguo Zhang, Anna Bergamaschi, Rebecca Barten, Camelia Borca, Giacomo Borghi, Maurizio Boscardin, Martin Brückner, Nicolás Cartiglia, Sabina Chiriotti, et al. Development of low-energy x-ray detectors using lgad sensors. *Journal of synchrotron radiation*, 26(4):1226–1237, 2019.
- [3] Niccolò Banterle, Khanh Huy Bui, Edward A. Lemke, and Martin Beck. Fourier ring correlation as a resolution criterion for super-resolution microscopy. *Journal of Structural Biology*, 183(3):363–367, 2013.
- [4] Julius S Bendat. Principles and applications of random noise theory. *Ramo-Wooldridge Corp., Los Angeles, USA, Printed John Wiley & Sons, New York, USA, Card Number 58-12705*, 1958.
- [5] A. Bergamaschi, S. Cartier, R. Dinapoli, D. Greiffenberg, J. H. Jungmann-Smith, D. Mezza, A. Mozzanica, B. Schmitt, X. Shi, and G. Tinti. Looking at single photons using hybrid detectors. *Journal of Instrumentation*, 10(1):C01033, January 2015.
- [6] Christian Brönnimann and Peter Trüb. Hybrid pixel photon counting x-ray detectors for synchrotron radiation. *Synchrotron Light Sources and Free-Electron Lasers: Accelerator Physics, Instrumentation and Science Applications*, pages 1191–1223, 2020.
- [7] Tim A. Butcher, Nicholas W. Phillips, Chun-Chien Chiu, Chia-Chun Wei, Sheng-Zhu Ho, Yi-Chun Chen, Erik Fröjdh, Filippo Baruffaldi, Maria Carulla, Jiaguo Zhang, Anna Bergamaschi, Carlos A. F. Vaz, Armin Kleibert, Simone Finizio, Jan-Chi Yang, Shih-Wen Huang,



and Jörg Raabe. Ptychographic nanoscale imaging of the magnetoelectric coupling in freestanding BiFeO<sub>3</sub>. *Advanced Materials*, 36(23):2311157, 2024.

- [8] Tim A. Butcher, Nicholas W. Phillips, Chia-Chun Wei, Shih-Chao Chang, Igor Beinik, Karina Thånell, Jan-Chi Yang, Shih-Wen Huang, Jörg Raabe, and Simone Finizio. Imaging ferroelectric domains with soft-x-ray ptychography at the oxygen k-edge. *Phys. Rev. Appl.*, 23:L011002, Jan 2025.
- [9] N Cartiglia, R Arcidiacono, G Borghi, M Boscardin, M Costa, Z Galloway, F Fausti, M Ferrero, F Ficorella, M Mandurrino, et al. Lgad designs for future particle trackers. *Nuclear Instruments and Methods in Physics Research Section A: Accelerators, Spectrometers, Detectors and Associated Equipment*, 979:164383, 2020.
- [10] M. Carulla, A. Doblas, D. Flores, Z. Galloway, S. Hidalgo, G. Kramberger, Z. Luce, I. Mandic, S. Mazza, A. Merlos, G. Pellegrini, D. Quirion, R. Rodríguez, H.F.-W. Sadrozinski, A. Seiden, and Y. Zhao. 50  $\mu\text{m}$  thin low gain avalanche detectors (lgad) for timing applications. *Nuclear Instruments and Methods in Physics Research Section A: Accelerators, Spectrometers, Detectors and Associated Equipment*, 924:373–379, 2019. 11th International Hiroshima Symposium on Development and Application of Semiconductor Tracking Detectors.
- [11] Maria Carulla, Rebecca Barten, Filippo Baruffaldi, Anna Bergamaschi, Giacomo Borghi, Maurizio Boscardin, Martin Brückner, Tim A Butcher, Matteo Centis Vignali, Roberto Dinapoli, et al. Quantum efficiency measurement and modeling of silicon sensors optimized for soft x-ray detection. *Sensors*, 24(3):942, 2024.
- [12] Arnau Casanas, Rangana Warshamanage, Aaron D Finke, Ezequiel Panepucci, Vincent Olieric, Anne Nöll, Robert Tampé, Stefan Brandstetter, Andreas Förster, Marcus Mueller, et al. Eiger detector: application in macromolecular crystallography. *Acta Crystallographica Section D: Structural Biology*, 72(9):1036–1048, 2016.
- [13] Matteo Centis Vignali and Giovanni Paternoster. Low gain avalanche diodes for photon science applications. *Frontiers in Physics*, 12, 2024.
- [14] Silvia Cipiccia, Michela Fratini, Ecem Erin, Marco Palombo, Silvia Vogel, Max Burian, Fenglei Zhou, Geoffrey Parker, and Darren Batey. Fast x-ray ptychography: towards nanoscale imaging of large volume of brain. *The European Physical Journal Plus*, 139, 05 2024.
- [15] Brian A Collins and Eliot Gann. Resonant soft x-ray scattering in polymer science. *Journal of Polymer Science*, 60(7):1199–1243, 2022.
- [16] G. F. Dalla Betta, Lucio Pancheri, Maurizio Boscardin, Giovanni Paternoster, Claudio Piemonte, Nicolo Cartiglia, Francesca Cenna, and Mara Bruzzi. Design and tcad simulation of double-sided pixelated low gain avalanche detectors. *Nuclear Instruments and Methods in Physics Research Section A: Accelerators, Spectrometers, Detectors and Associated Equipment*, 796:154–157, 2015.

- [17] Kewin Desjardins, Kadda Medjoubi, Maurizio Sacchi, Horia Popescu, Roland Gaudemer, Rachid Belkhou, Stefan Stanescu, Sufal Swaraj, Adrien Besson, Jaianth Vijayakumar, et al. Backside-illuminated scientific cmos detector for soft x-ray resonant scattering and ptychography. *Journal of Synchrotron Radiation*, 27(6):1577–1589, 2020.
- [18] Kewin Desjardins, Horia Popescu, Pascal Mercère, Claude Meneglier, Roland Gaudemer, Karina Thänell, and Nicolas Jaouen. Characterization of a back-illuminated CMOS camera for soft x-ray coherent scattering. *AIP Conference Proceedings*, 2054(1), 2019.
- [19] Roberto Dinapoli, Anna Bergamaschi, Dominic Greiffenberg, Beat Henrich, Roland Horisberger, Ian Johnson, Aldo Mozzanica, Valeria Radicci, Bernd Schmitt, Xintian Shi, et al. Eiger characterization results. *Nuclear Instruments and Methods in Physics Research Section A: Accelerators, Spectrometers, Detectors and Associated Equipment*, 731:68–73, 2013.
- [20] Kamel El Omari, Ramona Duman, Vitaliy Mykhaylyk, Christian M Orr, Merlyn Latimer-Smith, Graeme Winter, Vinay Grama, Feng Qu, Kiran Bountra, Hok Sau Kwong, et al. Experimental phasing opportunities for macromolecular crystallography at very long wavelengths. *Communications Chemistry*, 6(1):219, 2023.
- [21] Hebatalla Elnaggar, RuPan Wang, Mahnaz Ghiasi, Maria Yañez, Mario U Delgado-Jaime, Mai Hussein Hamed, Amélie Juhin, Sarnjeet S Dhesi, and Frank de Groot. Probing the local distortion of fe sites in fe 3 o 4 thin films using enhanced symmetry selection in xmdl. *Physical Review Materials*, 4(2):024415, 2020.
- [22] Andreas Förster, Stefan Brandstetter, and Clemens Schulze-Briese. Transforming x-ray detection with hybrid photon counting detectors. *Philosophical Transactions of the Royal Society A*, 377(2147):20180241, 2019.
- [23] Erik Fröjd, Anna Bergamaschi, and Bernd Schmitt. Single-photon counting detectors for diffraction-limited light sources. *Frontiers in Physics*, 12, 2024.
- [24] B Henrich, A Bergamaschi, C Broennimann, R Dinapoli, EF Eikenberry, I Johnson, M Kobas, P Kraft, A Mozzanica, and B Schmitt. Pilatus: A single photon counting pixel detector for x-ray applications. *Nuclear Instruments and Methods in Physics Research Section A: Accelerators, Spectrometers, Detectors and Associated Equipment*, 607(1):247–249, 2009.
- [25] JT Heron, JL Bosse, Q He, Y Gao, Morgan Trassin, L Ye, JD Clarkson, C Wang, Jian Liu, S Salahuddin, et al. Deterministic switching of ferromagnetism at room temperature using an electric field. *Nature*, 516(7531):370–373, 2014.
- [26] V. Hinger, A. al Haddad, R. Barten, A. Bergamaschi, M. Bruckner, M. Carulla, S. Chiriotti, R. Dinapoli, S. Ebner, E. Fröjd, D. Greiffenberg, S. Hasanaaj, T. King, P. Kozlowski, C. Lopez-Cuenca, D. Mezza, K. Moustakas, A. Mozzanica, D. Ozerov, C. Ruder, B. Schmitt, K.A. Schnorr, D. Thattil, and J. Zhang. Advancing the

- JUNGFRAU detector toward low-energy x-ray applications. *Journal of Instrumentation*, 17:C09027, 2022.
- [27] Viktoria Hinger, Rebecca Barten, Filippo Baruffaldi, Anna Bergamaschi, Giacomo Borghi, Maurizio Boscardin, Martin Brückner, Maria Carulla, Matteo Centis Vignali, Roberto Dinapoli, et al. Resolving soft x-ray photons with a high-rate hybrid pixel detector. *Frontiers in Physics*, 12:1352134, 2024.
- [28] Adam P Hitchcock. Soft x-ray spectromicroscopy and ptychography. *Journal of Electron Spectroscopy and Related Phenomena*, 200:49–63, 2015.
- [29] Samy Hocine, Helena Van Swygenhoven, Steven Van Petegem, Cynthia Sin Ting Chang, Tuerdi Maimaitiyili, Gemma Tinti, Dario Ferreira Sanchez, Daniel Grolimund, and Nicola Casati. Operando x-ray diffraction during laser 3d printing. *Materials Today*, 34:30–40, 2020.
- [30] Mirko Holler, Michal Odstrcil, Manuel Guizar-Sicairos, Maxime Lebugle, Elisabeth Müller, Simone Finizio, Gemma Tinti, Christian David, Joshua Zusman, Walter Unglaub, et al. Three-dimensional imaging of integrated circuits with macro-to nanoscale zoom. *Nature Electronics*, 2(10):464–470, 2019.
- [31] A Khromova, G Cautero, D Giuressi, R Menk, Giovanni Pinaroli, L Stebel, J Correa, A Marras, CB Wunderer, S Lange, et al. Report on recent results of the percival soft x-ray imager. *Journal of Instrumentation*, 11(11):C11020, 2016.
- [32] P Kraft, A Bergamaschi, Ch Broennimann, R Dinapoli, EF Eikenberry, B Henrich, I Johnson, A Mozzanica, CM Schlepütz, PR Willmott, et al. Performance of single-photon-counting pilatus detector modules. *Journal of synchrotron radiation*, 16(3):368–375, 2009.
- [33] M. Langer, S. Vaz, C. A. F. and Chiriotti, A. Bergamaschi, M. Guizar-Sicairos, A. Kleibert, and J. Raabe. Development of a new soft x-ray ptychography spectro-microscope at the swiss light source (sls). *Microscopy & Microanalysis*, 24:54–55, 2018.
- [34] Antonio Liguori, Rebecca Barten, Filippo Baruffaldi, Anna Bergamaschi, Giacomo Borghi, Maurizio Boscardin, Martin Brückner, Tim Alexander Butcher, Maria Carulla, Matteo Centis Vignali, et al. Characterization of ilgads using soft x-rays. *Journal of Instrumentation*, 18(12):P12006, 2023.
- [35] Feng Liu, Michael A Brady, and Cheng Wang. Resonant soft x-ray scattering for polymer materials. *European Polymer Journal*, 81:555–568, 2016.
- [36] K. Mathieson, M. S. Passmore, P. Seller, M. L. Prydderch, V. O’Shea, R. L. Bates, K. M. Smith, and M. Rahman. Charge sharing in silicon pixel detectors. *Nucl. Instrum. Meth. A*, 487:113–122, 2002.
- [37] Nicolas Mille, Hao Yuan, Jaianth Vijayakumar, Stefan Stanescu, Sufal Swaraj, Kewin Desjardins, Vincent Favre-Nicolin, Rachid Belkhou, and Adam P Hitchcock. Ptychography at the carbon k-edge. *Communications Materials*, 3(1):8, 2022.

- [38] Michal Odstrčil, Andreas Menzel, and Manuel Guizar-Sicairos. Iterative least-squares solver for generalized maximum-likelihood ptychography. *Opt. Express*, 26(3):3108–3123, Feb 2018.
- [39] Kamil Olejník, Tom Seifert, Zdeněk Kašpar, Vít Novák, Peter Wadley, Richard P Champion, Manuel Baumgartner, Pietro Gambardella, Petr Němec, Joerg Wunderlich, et al. Terahertz electrical writing speed in an antiferromagnetic memory. *Science advances*, 4(3):eaar3566, 2018.
- [40] G Paternoster, G Borghi, Roberta Arcidiacono, M Boscardin, N Cartiglia, M Centis Vignali, GF Dalla Betta, M Ferrero, F Ficorella, M Mandurrino, et al. Novel strategies for fine-segmented low gain avalanche diodes. *Nuclear Instruments and Methods in Physics Research Section A: Accelerators, Spectrometers, Detectors and Associated Equipment*, 987:164840, 2021.
- [41] Giulio Pellegrini, Pablo Fernández-Martínez, Marta Baselga, Celeste Fleta, D Flores, Virginia Greco, Salvador Hidalgo, I Mandić, G Kramberger, David Quirion, et al. Technology developments and first measurements of low gain avalanche detectors (lgad) for high energy physics applications. *Nuclear Instruments and Methods in Physics Research Section A: Accelerators, Spectrometers, Detectors and Associated Equipment*, 765:12–16, 2014.
- [42] Franz Pfeiffer. X-ray ptychography. *Nature Photonics*, 12(1):9–17, 2018.
- [43] H Popescu, J Perron, B Pilette, R Vacheresse, V Pinty, R Gaudemer, Maurizio Sacchi, R Delaunay, F Fortuna, K Medjoubi, et al. Comet: a new end-station at soleil for coherent magnetic scattering in transmission. *Journal of Synchrotron Radiation*, 26(1):280–290, 2019.
- [44] C Quitmann, U Flechsig, L Patthey, T Schmidt, G Ingold, M Howells, M Janousch, and R Abela. A beamline for time resolved photoelectron microscopy on magnetic materials at the swiss light source. *Surface Science*, 480(3):173–179, 2001.
- [45] Veljko Radeka. Low-noise techniques in detectors. *Annual Review of Nuclear and Particle Science*, 38(1):217–277, 1988.
- [46] V Radicci, A Bergamaschi, R Dinapoli, D Greiffenberg, B Henrich, I Johnson, A Mozzanica, B Schmitt, and X Shi. Eiger a new single photon counting detector for x-ray applications: performance of the chip. *Journal of Instrumentation*, 7(02):C02019, 2012.
- [47] S Redford, A Bergamaschi, M Brückner, S Cartier, R Dinapoli, Y Ekinici, E Fröjd, D Greiffenberg, D Mayilyan, D Mezza, et al. Calibration status and plans for the charge integrating jungfrau pixel detector for swissfel. *Journal of Instrumentation*, 11(11):C11013, 2016.
- [48] L Rota, C Tamma, JD Segal, P Caragiulo, C Kenney, and A Dragone. Design of epixm, a fully-depleted monolithic cmos active pixel sensor for soft x-ray experiments at lcls-ii. *Journal of Instrumentation*, 14(12):C12014, 2019.

- [49] HF-W Sadrozinski, S Ely, V Fadeyev, Z Galloway, J Ngo, C Parker, B Petersen, A Seiden, A Zatserklyaniy, N Cartiglia, et al. Ultrafast silicon detectors. *Nuclear Instruments and Methods in Physics Research Section A: Accelerators, Spectrometers, Detectors and Associated Equipment*, 730:226–231, 2013.
- [50] V Scagnoli, U Staub, Y Bodenthin, RA De Souza, M García-Fernández, M Garganourakis, AT Boothroyd, D Prabhakaran, and SW Lovesey. Observation of orbital currents in cuo. *Science*, 332(6030):696–698, 2011.
- [51] J. Schwenke, K. Thånell, I. Beinik, L. Roslund, and T. Tylliszczak. Soft/max-a new soft x-ray microscopy and coherent imaging beamline at the max iv facility. *Microscopy & Microanalysis*, 24:232–233, 2018.
- [52] W Snoeys. Monolithic pixel detectors for high energy physics. *Nuclear Instruments and Methods in Physics Research Section A: Accelerators, Spectrometers, Detectors and Associated Equipment*, 731:125–130, 2013.
- [53] MR Soman, DJ Hall, JH Tutt, NJ Murray, AD Holland, T Schmitt, J Raabe, and B Schmitt. Developing a ccd camera with high spatial resolution for rixs in the soft x-ray range. *Nuclear Instruments and Methods in Physics Research Section A: Accelerators, Spectrometers, Detectors and Associated Equipment*, 731:47–52, 2013.
- [54] Lothar Strüder, Sascha Epp, Daniel Rolles, Robert Hartmann, Peter Holl, Gerhard Lutz, Heike Soltau, Rouven Eckart, Christian Reich, Klaus Heinzinger, et al. Large-format, high-speed, x-ray pnccds combined with electron and ion imaging spectrometers in a multipurpose chamber for experiments at 4th generation light sources. *Nuclear Instruments and Methods in Physics Research Section A: Accelerators, Spectrometers, Detectors and Associated Equipment*, 614(3):483–496, 2010.
- [55] Pierre Thibault, Martin Dierolf, Andreas Menzel, Oliver Bunk, Christian David, and Franz Pfeiffer. High-resolution scanning x-ray diffraction microscopy. *Science*, 321(5887):379–382, 2008.
- [56] Pierre Thibault and Andreas Menzel. Reconstructing state mixtures from diffraction measurements. *Nature*, 494(7435):68–71, February 2013.
- [57] Gemma Tinti, Anna Bergamaschi, S. Cartier, Roberto Dinapoli, Dominic Greiffenberg, I. Johnson, Julia Smith, Davide Mezza, Aldo Mozzanica, B. Schmitt, and Xintian Shi. Performance of the eiger single photon counting detector. *Journal of Instrumentation*, 10:C03011–C03011, 03 2015.
- [58] James H Tutt, Andrew D Holland, Neil J Murray, David J Hall, Richard D Harriss, Andrew Clarke, and Anthony M Evagora. The noise performance of electron-multiplying charge-coupled devices at soft x-ray energy values. *IEEE Transactions on Electron Devices*, 59(8):2192–2198, 2012.

- [59] Gerrit van der Laan and Adriana I Figueroa. X-ray magnetic circular dichroism—a versatile tool to study magnetism. *Coordination Chemistry Reviews*, 277:95–129, 2014.
- [60] Armin Wagner, Ramona Duman, Keith Henderson, and Vitaliy Mykhaylyk. In-vacuum long-wavelength macromolecular crystallography. *Acta Crystallographica Section D: Structural Biology*, 72(3):430–439, 2016.
- [61] Klaus Wakonig, Hans-Christian Stadler, Michal Odstrčil, Esther H. R. Tsai, Ana Diaz, Mirko Holler, Ivan Usov, Jörg Raabe, Andreas Menzel, and Manuel Guizar-Sicairos. *PtychoShelves*, a versatile high-level framework for high-performance analysis of ptychographic data. *J. Appl. Cryst.*, 53(2):574–586, Apr 2020.
- [62] Jan Wernecke, Christian Gollwitzer, Peter Müller, and Michael Krumrey. Characterization of an in-vacuum pilatus 1m detector. *Journal of Synchrotron Radiation*, 21(3):529–536, 2014.
- [63] Anna M Wise, Johanna Nelson Weker, Sam Kalirai, Maryam Farmand, David A Shapiro, Florian Meirer, and Bert M Weckhuysen. Nanoscale chemical imaging of an individual catalyst particle with soft x-ray ptychography. *ACS catalysis*, 6(4):2178–2181, 2016.
- [64] Young-Sang Yu, Maryam Farmand, Chunjoong Kim, Yijin Liu, Clare P Grey, Fiona C Stobridge, Tolek Tyliczszak, Rich Celestre, Peter Denes, John Joseph, et al. Three-dimensional localization of nanoscale battery reactions using soft x-ray tomography. *Nature communications*, 9(1):921, 2018.
- [65] P. Zambon, J. Vávra, G. Montemurro, S. Bottinelli, A. Dudina, R. Schnyder, C. Hörmann, M. Meffert, C. Schulze-Briese, D. Stroppa, N. Lehmann, and L. Piazza. High-frame rate and high-count rate hybrid pixel detector for 4d stem applications. *Frontiers in Physics*, 11, 2023.
- [66] Jianguo Zhang, Rebecca Barten, Filippo Baruffaldi, Anna Bergamaschi, Giacomo Borghi, Maurizio Boscardin, Martin Brueckner, Maria Carulla, M Centis Vignali, Roberto Dinapoli, et al. Development of lgad sensors with a thin entrance window for soft x-ray detection. *Journal of Instrumentation*, 17(11):C11011, 2022.
- [67] T Zinn, A Homs, L Sharpnack, G Tinti, E Fröjdh, P-A Douissard, M Kocsis, J Möller, Y Chushkin, and T Narayanan. Ultra-small-angle x-ray photon correlation spectroscopy using the eiger detector. *Journal of synchrotron radiation*, 25(6):1753–1759, 2018.

## Acknowledgements

Measurements with soft X-rays were performed at the Surface/Interface Microscopy (SIM-X11MA) beamline of the Swiss Light Source (SLS), Paul Scherrer Institut, Villigen, Switzerland. Additionally, soft X-ray ptychography measurements were carried out with the SOPHIE endstation at the SoftiMAX beamline of the MAX IV Laboratory. The SOPHIE endstation was designed and assembled at the Swiss Light Source

(SLS), Paul Scherrer Institut (PSI), Villigen, Switzerland. Research conducted at MAX IV, a Swedish national user facility, is supported by the Swedish Research council under contract 2018-07152, the Swedish Governmental Agency for Innovation Systems under contract 2018-04969, and Formas under contract 2019-02496. T.A.B. acknowledges funding from the Swiss Nanoscience Institute (SNI) and the European Regional Development Fund (ERDF). N.W.P. received funding from the European Union's Horizon 2020 research and innovation programme under the Marie Skłodowska-Curie grant agreement no. 884104. We thank Claire Donnelly for the fabrication of the permalloy Siemens star, Chia-Chun Wei, Shih-Wen Huang and Jan-Chi Yang for the fabrication and characterization of the freestanding BiFeO<sub>3</sub> film. We thanks Armin Kleibert and Carlos Vaz for the support at the SIM beamline of the Swiss Light Source. We additionally thank Karina Thånell and Igor Beinik for support at the SoftiMAX beamline at Max IV.

## Author contributions

Conceptualization: F.B., A.B. Methodology: F.B., A.B., M. Bo., M. Br., M.C., M.C.V., R.D., D.G., E.F., A.M., G.P., J.Z. Investigation: F.B., A.B., T.A.B., S.F., E.F., N.W.P. Visualization: F.B., T.A.B., S.F. Funding acquisition: A.B., B.S. Project administration: A.B., B.S. Supervision: A.B., J.R., B.S.

## Competing interests

The authors declare that they have no known competing financial interests or personal relationships that could have appeared to influence the work reported in this paper.

## Correspondence

Correspondence and requests for materials should be addressed to Anna Bergamaschi, [anna.bergamaschi@psi.ch](mailto:anna.bergamaschi@psi.ch).

# Single-photon counting pixel detector for soft X-rays

## Supplementary Material

Filippo Baruffaldi<sup>1,4</sup>, Anna Bergamaschi<sup>1</sup>, Maurizio Boscardin<sup>2</sup>, Martin Brückner<sup>1</sup>, Tim A. Butcher<sup>1,3</sup>, Maria Carulla<sup>1</sup>, Matteo Centis Vignali<sup>2</sup>, Roberto Dinapoli<sup>1</sup>, Simone Finizio<sup>1</sup>, Erik Fröjd<sup>1</sup>, Dominic Greiffenberg<sup>1</sup>, Aldo Mozzanica<sup>1</sup>, Giovanni Paternoster<sup>2</sup>, Nicholas W. Phillips<sup>1,5</sup>, Jörg Raabe<sup>1</sup>, Bernd Schmitt<sup>1</sup>, and Jianguo Zhang<sup>1</sup>

<sup>1</sup>Paul Scherrer Institut, Forschungsstrasse 111, 5232 Villigen PSI, Switzerland

<sup>2</sup>Fondazione Bruno Kessler, Via Sommarive 18, 38123 Trento, Italy

<sup>3</sup>Max Born Institute for Nonlinear Optics and Short Pulse Spectroscopy,  
Max-Born-Str. 2A, 12489 Berlin, Germany

<sup>4</sup>Present address: Dectris AG, Taefernweg 1, 5405 Baden-Dättwil, Switzerland

<sup>5</sup>Present address: CSIRO, Mineral Resources, CSIRO 3168, Australia

## S.1 Energy calibration

### Calibration Gain

Calibration and characterization of a single photon counting detector are typically performed by illuminating the detector with a monochromatic beam and acquiring images while scanning the comparator threshold, a process known as *threshold scan*. The number of counts  $N$ , as a function of the comparator threshold  $t$ , displayed in the top part of Fig. 7a, is referred to as the  $s$ -curve and represents the integral of the detected pulse-height distribution.

The uncalibrated pulse-height distributions shown in the lower part of Fig. 7a of the manuscript were obtained as the derivative of the average  $s$ -curves from approximately 5000 illuminated pixels, normalized by number of detected photons.

By fitting the  $s$ -curve with the equation obtained by applying a simplified linear charge collection model:

$$N(t) = N_0 \left( 1 + C_s \frac{t_0 - t}{\sigma} \right) \times \left( 1 + \operatorname{erf} \left( \frac{t_0 - t}{\sigma} \right) \right) \quad , \quad (\text{S1})$$

it is possible to estimate the threshold  $t_0$  corresponding to the photon energy used for the illumination, the effective noise  $\sigma$ , the number of detected photons  $N_0$  and the fraction of photons shared between multiple pixels  $C_s$  [? ].

The calibration gain  $\mathcal{G}$  and the comparator baseline  $q$  can be extracted by a linear fit of the  $t_0$  obtained for different beam energies:

$$t_0(E) = \mathcal{G}E + q \quad . \quad (\text{S2})$$

The calibration parameters  $\mathcal{G}$  and  $q$  depend on the gain settings of the preamplifier and the multiplication factor of the LGAD sensor  $M$ , and they are individually estimated for each pixel. The calibrated pulse-height distributions shown in Figure 2 of the manuscript were obtained by converting the threshold into energy on a pixel-by-pixel basis, then calculating the derivative of the summed calibrated  $s$ -curves from approximately 2000 pixels illuminated by the beam.



The settings of the readout electronics were adjusted in different measurements by tuning  $vrpreamp$  to match the dynamic range of the preamplifier with the iLGAD gain and the photon energy. All data presented in Figure 7a were acquired using 900 eV X-rays with the same settings of the read-out electronics ( $vrpreamp=1700$  mV), across the various sensor variations. Data in Fig2a,b were collected with  $vrpreamp$  settings individually optimized for the photon energy and sensor variation: with the *shallow* variation  $vrpreamp=1750$  mV was used for the energies 650 eV and above,  $vrpreamp=1850$  mV for 550 eV and 600 eV. The setting  $vrpreamp=1700$  mV was used with the *standard* variation for all the shown energies.

The iLGAD multiplication factor  $M$  is estimated as the ratio between the average  $\mathcal{G}$  of the LGAD-based detector and that of the EIGER detector with a conventional silicon sensor, using the same gain settings. The calibration gain  $\mathcal{G}$  and estimated multiplication factor  $M$  for the various iLGAD variations considered are listed in Table S1.

## Noise and Signal-to-Noise Ratio

The electronic noise is best described in terms of Equivalent Noise Charge (ENC) i.e., the amount of charge needed at the detector input to create an output signal at the end of the analogue chain equivalent to the measured noise [?]. It is possible to estimate the effective noise in a single photon counting detector by converting the parameter  $\sigma$  obtained from the fit of the  $s$ -curve according to equation S1 expressed either in eV or in electrons with:

$$\begin{aligned}\sigma[eV] &= \frac{\sigma[mV]}{\mathcal{G}} \quad , \\ \sigma[e^-] &= \frac{\sigma[eV]}{3.6 \text{ eV}} \quad ,\end{aligned}\tag{S3}$$

where  $\mathcal{G}$  is the calibration gain obtained from the linear fit according to equation S2, and 3.6 eV is the average electron-hole pair generation energy in silicon. The noise values are calculated individually for each pixel and averaged. The noise values displayed in Fig 4a in the manuscript are reported in Table S1, with the errors indicating the standard deviation of pixels distribution. The noise reduction factors, shown in Fig. 4b, are obtained as the ratios between the noise values of the conventional sensor and the iLGAD variation, considering the same settings. The energy used for the noise estimations are also reported in the table.

The Signal-to-Noise Ratio (SNR) is calculated for each pixel as:

$$\frac{S}{N} = \frac{t_0 - q}{\mathcal{G}} \frac{\mathcal{G}}{\sigma} = \frac{t_0 - q}{\sigma} \quad ;\tag{S4}$$

The average SNR and the error plotted in Fig. 3 are the mean and standard deviation obtained by fitting the SNR distribution of all pixels with a Gaussian. For each energy and sensor variation the optimal  $vrpreamp$  settings maximizing the SNR have been chosen.

## S.2 Detective Quantum Efficiency

The Detective Quantum Efficiency (DQE) is defined by the ratio of the squared output signal-to-noise ratio to the squared input signal-to-noise ratio of the imaging detector. For an ideal detector, the DQE coincides with the absorption Quantum Efficiency of the sensor. In Fig. 5b of the manuscript, the DQE is plotted as a function of photon energy, evaluated at zero spatial frequency without accounting for the spatial resolution. This DQE estimation uses a Monte Carlo approach, factoring in photon absorption depth, the LGAD multiplication process, charge sharing, and the electronics noise from the EIGER readout. Photon absorption profiles in silicon for monochromatic photons (550–900 eV) were simulated using the Geant4 Monte Carlo tool [?], and are used to

Variation	<i>vrpreamp</i> (mV)	ENC Noise ( $e^-$ )	$\mathcal{G}$ (mV/eV)	$M$	Energy (eV)
Conventional sensor	1400	$127.7 \pm 5.5$	$0.129 \pm 0.006$		8046
	1700	$81.0 \pm 4.8$	$0.241 \pm 0.023$		3000, 4000
Shallow $M=3.2$	1700	$26.3 \pm 3.6$	$0.76 \pm 0.12$	$3.15 \pm 0.57$	800-900
Shallow $M=4.8$	1700	$23.3 \pm 1.4$	$1.15 \pm 0.11$	$4.75 \pm 0.66$	700-900
Standard $M=6.1$	1700	$23.5 \pm 1.5$	$1.46 \pm 0.09$	$6.07 \pm 0.69$	550-900
Standard $M=10.7$	1400	$24.5 \pm 1.6$	$1.39 \pm 0.08$	$10.72 \pm 0.78$	815-1000

**Table S1: Calibration results.** Calibration gain  $\mathcal{G}$ , Equivalent Noised charge (ENC) values, iLGADS multiplication factor  $M$  for the characterized sensor variations, including a conventional silicon sensor. Data reported in this Table are summarized in Fig. 4a and b in the main manuscript. The *vrpreamp* settings used are also reported. The last columns refers to the energies at which the measurements were performed. The measurements with the conventional sensor at 8046 eV was performed with a fluorescence Cu target and a Ni  $K_\beta$ -filter, the remaining datasets were obtained with mono-energetic photon beams at the SLS synchrotron.

estimate the fraction of the photons that convert either before, within, or after the gain layer, as a function of the energy. Effective hole- and electron-initiated multiplication factors, gain layer thickness, and their respective uncertainties, estimated in [?] for both *shallow* and *standard* variations, were used in the calculations. The charge-sharing effect is modeled as a 2D Gaussian diffusion of the charge, centered at the photon impact position; the fraction of the charge collected by a pixel is calculated as the 2D integral of the Gaussian distribution inside the pixel area [?]. The effect of the charge-sharing is averaged, by considering a uniform distribution of the photons impact points across the pixel area. The readout electronics noise is modeled as a Gaussian blur applied after charge sharing, with  $\sigma$  derived from the measured noise values in Table S1.

To determine the size of the charge cloud, the weighted sum of squared deviations between measured and simulated pulse-height distributions for various charge cloud sizes was minimized. This yields optimal charge cloud sizes of  $7.16 \pm 0.15 \mu\text{m}$  for the *standard* iLGAD and  $5.05 \pm 0.16 \mu\text{m}$  for the *shallow* variation, with error bars corresponding to the  $\frac{\chi^2_0}{ndf} + 1$  [?]. Despite similar charge collection times expected for sensors of the same thickness and applied bias, the charge cloud size difference likely arises from voltage drops due to high leakage current and a non-ideal biasing scheme, resulting in different effective bias voltages for the two sensors. Moreover, the higher charge density in high-gain sensors can potentially lead to faster diffusion due to Coulomb repulsion. Figure S1 compares the pulse-height distributions acquired at various energies with the best fitting simulation.

The DQE in Figure 3b is calculated as the product of the absorption efficiency measured in [?] for the same iLGAD variation and the fraction of the photons exceeding both the half energy and the  $5\sigma$  threshold, considered as the minimum acceptable threshold for the proper operation of the detector.

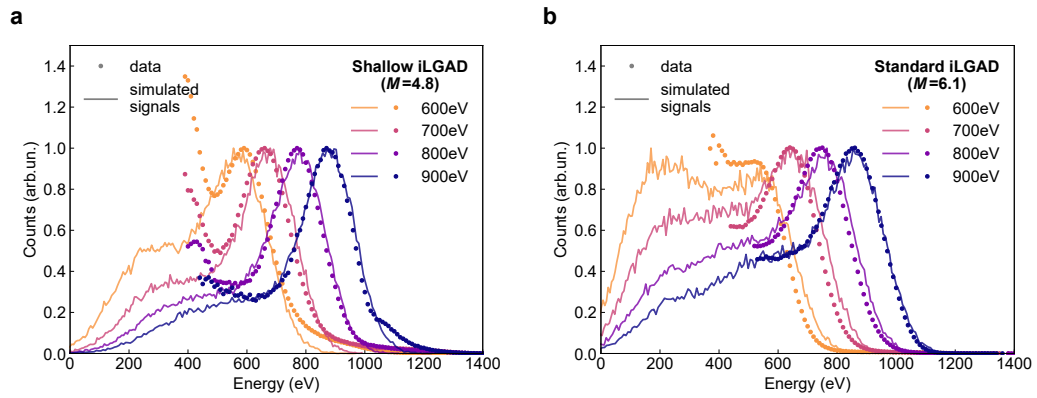


**Figure S1: Simulated vs. experimental pulse-height distributions. a** *Shallow* variation  $M=4.8$ ; charge cloud  $5.05 \pm 0.16 \mu\text{m}$ . **b** *Standard* variation  $M=6.1$ ; charge cloud  $7.16 \pm 0.15 \mu\text{m}$ .